Experimental assessment of Tomographic-PIV accuracy

G.E. Elsinga[1], B.W. van Oudheusden[1], F. Scarano[1]

[1] Dept. of Aerospace Engineering, Delft University of Technology, The Netherlands, g.e.elsinga@tudelft.nl

Abstract Tomographic-PIV is a recently developed three-dimensional velocimetry technique relying on the reconstruction of the instantaneous three-dimensional tracer particle distribution from their recorded images by means of a tomographic algorithm. Although previous experiments have shown good potential for the technique returning the expected 3D flow structure, the results so far have never been assessed quantitatively. Therefore the present study proposes an experimental investigation to quantify both 3D particle reconstruction noise and velocity accuracy in Tomographic-PIV. Measurements of a circular cylinder wake flow at $Re_D = 2700$ are carried out varying the most relevant experimental parameters, which are the light sheet thickness (ranging from 4 up to 12 mm) and particle image density (ranging from 0.01 to 0.1 *ppp*). From the returned reconstruction volumes the noise level (or ghost particle density) is extracted, which results in the reconstruction accuracy as a function of the mentioned experimental parameters. Based on this function the reconstruction accuracy in other experiments can be estimated. Finally the velocity accuracy is determined from a comparison with Stereo-PIV. It is shown that the mean and RMS velocity agree within 0.5 and 0.3 m/s respectively (corresponding to 0.30 and 0.18 voxel particle displacement). Furthermore it was found that reconstruction noise or ghost particles have a limited effect on the cross-correlation. For the range of particle image seeding densities considered (0.02 to 0.08 *ppp*) no significant difference in the returned flow statistics was observed, even though the number of ghost particles exceeded the number of actual particle for 0.08 *ppp*.

1. Introduction

The measurement of the three-dimensional velocity field is expected to give an important contribution to fluid dynamic research, because it is able visualize the instantaneous flow structure. Thereto several 3D PIV techniques have been developed such as Holographic-PIV (Hinsch 2002), scanning light sheet PIV (Brücker 1995), 3D-PTV (Maas et al. 1993) and Tomographic-PIV (Elsinga et al. 2005a, 2006). The latter is a recently developed technique that records the tracer particle images from several directions simultaneously and uses tomography to reconstruct the particle distribution within the illuminated volume as a 3D light intensity map. From cross-correlation of two 3D intensity maps corresponding to subsequent exposures of the particle images the velocity field is obtained.

The application of Tomographic-PIV to a cylinder wake flow in a wind tunnel showed that the technique was capable of measuring the instantaneous velocity distribution in a 30.9x25.8x6 mm^3 volume. Moreover the flow variations in depth were well captured (Elsinga et al. 2005b). The experiment results demonstrated good potential for the technique, however, the assessment was only qualitative and questions concerning the accuracy of the tomographic reconstruction and velocity measurement remained to be addressed.

Therefore the present study proposes an experimental investigation to quantify reconstruction noise and velocity accuracy in Tomographic-PIV. The most important source of error that is specific to photogrammetric 3D-PIV techniques is related to ghost particles, which form when the particle images from all recordings triangulate in points in the volume where there is physically no particle present (see section 2). As stated by Maas et al. (1993) the number of ghost particles is determined mainly by three experimental parameters: the number of cameras, the tracer particle density and the light sheet or volume thickness. Therefore in the present study the number of ghost

particles and their peak intensity are determined as functions of these parameters (section 4). Based on this information combined with the velocity of the ghost particles, the contribution of the ghost particles to the cross-correlation map and consequently the accuracy of the velocity measurement can be assessed (section 5). Furthermore the average velocity distribution is compared with results from (scanning) Stereo-PIV, which serves as the technique of reference in the present study.

2. Formation of ghost particles

The formation of ghost particles, or reconstruction noise, is illustrated in figure 1 for a 2-camera system. The measurement volume contains two particles, which are seen by camera 1 along the lines-of-sight LOS_1 and LOS_2 and by camera 2 along the lines LOS_3 and LOS_4. The recorded particle images are used by the tomographic reconstruction algorithm to determine the particle distribution in the measurement volume. Particles are formed at the intersections of a lines-of-sight from each camera corresponding to a particle (i.e. *LOS* 1-4). The lines triangulate in four points resulting in three possible solutions for the particle reconstruction (fig. 2). It can be shown that the present tomographic reconstruction algorithm converges to the 4-particle solution shown in figure 2C. The particles have equal intensity. Two of the reconstructed particles correspond to actual tracer particle and two are ghost particle or noise peaks in the reconstruction (fig. 1).

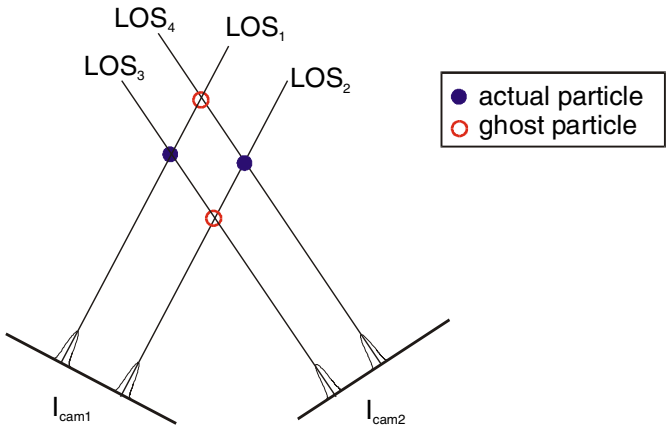

Figure 1: Formation of ghost particles in a 2 camera setup.

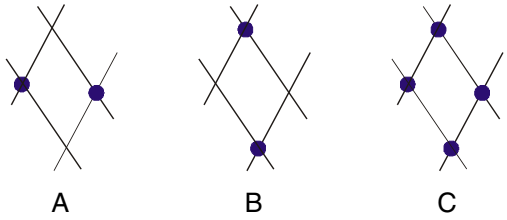

Figure 2: Reconstruction solutions to the 2-particle-2camera problem of figure 1.

In the general case of an *N*-camera system, a particle (either ghost or actual particle) is reconstructed in a point in the volume, when each of the *N* lines-of-sight going through that point corresponds to a particle image in the respective *N* recordings. Assuming ghost particle formation is a random process, the chance that a point in the volume corresponds to a particle image in each recordings is $\left(ppp \cdot A_p\right)^N$, where *ppp* (particles per pixel) is the particle density in the recordings and

A_p is the particle image area in pixel units. Then the total number of ghost particles N_g in the measurement volume is given by:

$$N_g = \left(ppp \cdot A_p \right)^N \cdot l_x \cdot l_y \cdot l_z \tag{1}$$

where $l_x \cdot l_y \cdot l_z$ are the dimensions of the reconstruction volume in x, y and z direction in voxel units (width, height and thickness). The number of actual tracer particles in the volume N_p is estimated by:

$$N_p = ppp \cdot l_x \cdot l_y \tag{2}$$

It is assumed that the pixels and voxels have equal dimensions and that the entire volume can be imaged onto $l_x \cdot l_y$ pixels. The thickness l_z of the volume usually is much smaller than its height and width. The signal-to-noise ratio in the tomographic reconstruction of the 3D particle distribution is expressed by the ratio of the actual tracer particle of the number of ghost particles N_p/N_g:

$$\frac{N_p}{N_g} = \frac{1}{ppp^{N-1} \cdot A_p{}^N \cdot l_z} \tag{3}$$

From the equation it is seen that the signal-to-noise ratio in the reconstruction strongly depends on the particle image density expressed in *ppp*. With decreasing *ppp* the chance of random intersections of lines-of-sight corresponding to particle images rapidly decreases, hence the number of ghost particles drops. The ratio N_p/N_g furthermore depends on the depth of the reconstruction volume, which is proportional to the interception length of the line-of-sight with the volume. Finally the particle image area A_p is usually a constant in a given experimental setup, which depends mainly on the optical settings (i.e. $f_\#$).

In the following experimental assessment of the reconstruction accuracy both *ppp* and volume thickness l_z will be varied and results will be compared with the theoretical prediction of Eq. 3.

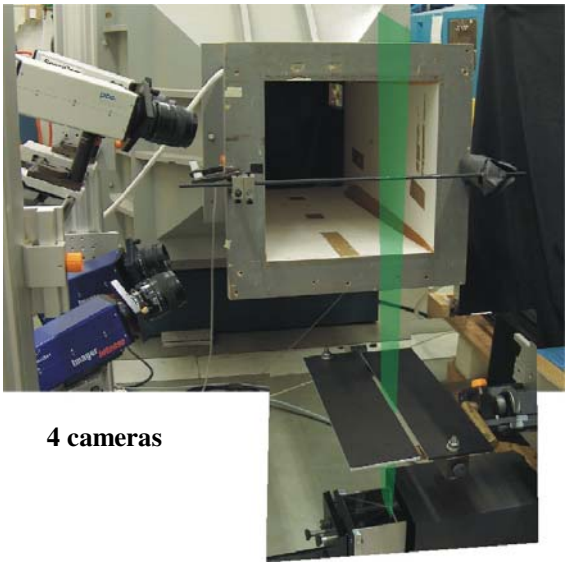

Figure 3: Experimental arrangement in the open-jet low speed wind tunnel

3. Experimental setup

The performance of Tomographic-PIV is assessed by measurements of a cylinder wake flow, which are conducted in a low-speed open-jet wind tunnel of Delft University of Technology at a free-stream velocity of 5 m/s. The wind tunnel has a 40x40 cm^2 square cross-section in which a circular cylinder of 8 mm diameter is placed horizontally (fig. 3). The corresponding Reynolds number based on the diameter is 2700.

The flow is seeded with 1 µm water droplets, which are illuminated by a Nd:YAG laser with 400 mJ per light pulse. The time separation between the pulses is 35 µs yielding a particle displacement of 0.18 mm (corresponding to 3.2 voxels) in the free-stream. The laser sheet is oriented vertically at 90 degrees angle with the cylinder axis. Compared to the previous cylinder wake experiments (Elsinga et al. 2005b) a slit is added in the path of the laser light sheet (fig. 3), which cuts the low light intensity edges from the light profile. As a result the light profile is sharp in depth direction and the light sheet is easily located in the reconstructed volume, which can be seen in the top view of a reconstructed volume (fig. 4).

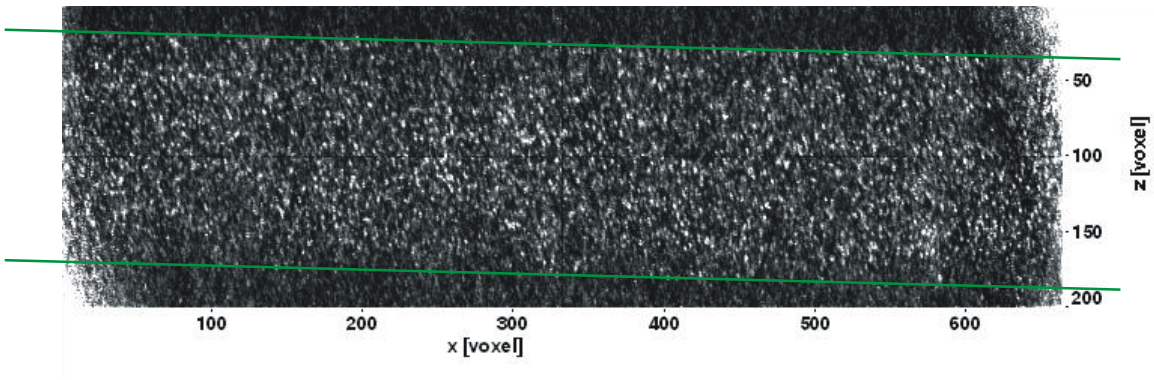

Figure 4: Top view of the reconstructed volume showing the light intensity integrated in y-direction. The green lines indicate the position of the 8 mm thick light sheet (0.03 ppp).

The particle images are recorded at 18.3 pixels/mm resolution using 4 CCD cameras in a rectangular configuration (fig. 3, 1 PCO SensiCam and 3 PCO SensiCam QE, 1280x1024 pixels, 12-bit). The viewing directions with respect to the cylinder axis (z-direction) are +/-22 degrees in vertical direction and –10 degrees (to the left) and +20 degrees (to the right) in the horizontal direction. The cameras are equipped with Nikon lenses using *f*/8 and Scheimpflug adapters to have the entire volume in focus. The imaging system is calibrated by fitting a 3rd order polynomial through the 15x 12 calibration marks in 3 planes separated 4 mm in z. The deviation between marks and fit is less than 0.2 pixel.

The recordings are pre-processed before reconstructing the volume. The background intensity is removed and the particle images are intensity normalized. Finally Gaussian smooth is applied (3x3 kernel size).

The intensity distribution in the measurement volume is reconstructed at 18.2 voxels/mm resolution using the multiplicative algebraic reconstruction technique (MART) as described in Elsinga et al. (2005a, 2006) with a relaxation parameter of 1. After 5 iterations the tomographic reconstruction is stopped, because the intensity distribution, hence the measured velocity, changes only within the noise level. The particle displacement is obtained using a 3D FFT-based cross-correlation algorithm with iterative multigrid and window deformation (Scarano and Riethmuller 2000).

Measurements are performed for varying light sheet thickness (2, 4, 8 and 12 mm) and seeding density level (ranging from 0.01 to 0.1 ppp) to determine the effect of each experimental parameter on the accuracy of Tomographic-PIV. The width and height of the measurement volume is kept constant at 36.5 and 35.8 mm respectively (667x654 voxels). The particle image density in the recordings is evaluated by counting intensity peaks above a threshold (9 counts, after background subtraction).

Two cameras from the above imaging system are used to return Stereo-PIV results for the 2 mm light sheet. Self-calibration on the particle images (Wieneke 2005) is applied to improve the Stereo-PIV results. Because the mean flow repeats itself along the cylinder axis, a single plane is sufficient to measure the mean flow properties (average and RMS velocities) thus a scanning light sheet system is not necessary. The mean flow thus obtained will be compared with Tomographic-PIV, for which the measured velocity is expected to be uniform in z (the direction of the cylinder axis).

4. Assessment reconstruction accuracy

Because ghost particles are formed when the particle images from all recordings triangulate in points where there is physically no particle, they can occur anywhere in the reconstructed volume with a constant probability, also outside the light sheet. Consequently the reconstructed intensity distribution outside and inside the light sheet represents the reconstruction noise (ghosts) and actual particles plus noise respectively. The ghost particle density can therefore be determined by counting the intensity peaks outside the light sheet. The corresponding intensity values return the PDF of the ghost particle peak intensity. The same procedure is followed inside the light sheet returning the particle density and peak intensity of the actual and ghost particles combined. Finally the difference (inside the light sheet minus outside) provides the values for the actual particles in the reconstruction. In the particle detection the volume is cropped to 560x550 voxels in x and y direction to remove border effects (fig. 4) and only intensity peaks above a threshold (5 counts) are counted. Furthermore the part of reconstructed volume outside the light sheet can be used to obtain information on the velocity of the ghost particle by cross-correlation (section 5).

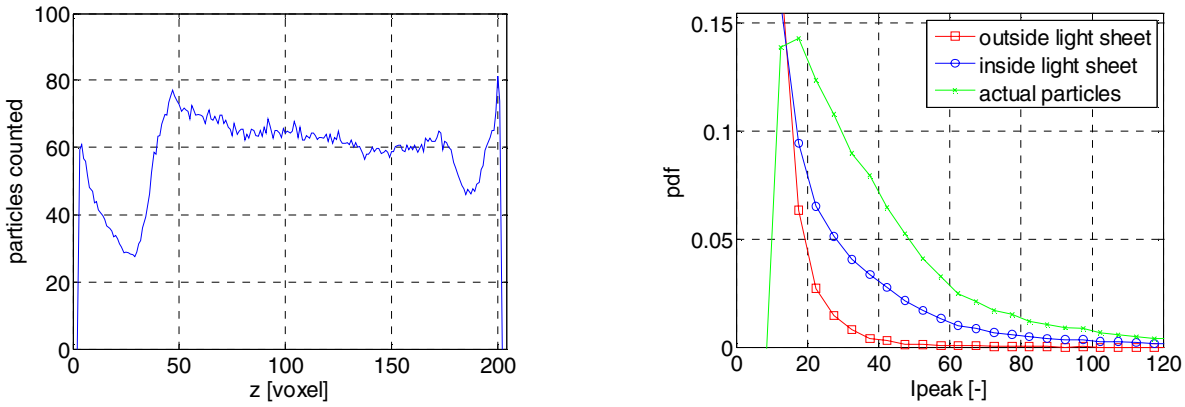

Figure 5: Distribution of intensity peaks in depth (left) and PDF of the peak intensity inside, outside the light sheet and actual particles (right) for an 8 mm thick light sheet and a seeding density of 0.019 ppp. The plots present results averaged over 40 reconstructed objects.

The distribution of the intensity peaks in the reconstructed volumes plotted against the depth-coordinate (fig. 5-left) shows that well inside the light sheet (z = [35, 185] voxels) there are on the

average 65 peaks or particles in each z-layer of the reconstructed volume, while outside (z = [20, 30] voxels) approximately 30 peaks are returned. Assuming the latter value is the ghost particle density, it is concluded that inside the light sheet there are 35 actual particles per unit depth, which means 54% of the intensity peaks correspond to actual tracer particles. Furthermore border effects are observed, which increase the number intensity peaks towards the edges of the volume. Note that such an effect is not observed in figure 4 (intensity integrated in y-direction), because the additional particles have a relatively low intensity. For z > 185 voxels the number of particles does not return to 30 per slice, because the light sheet is misaligned with the coordinate system so that part of the z-slice is still in the light sheet (fig. 4).

To check consistency between the number of particles in the recordings and in the reconstruction, the total number of particles in the considered volume is computed. Based on the recordings the total number of particles is $ppp \cdot l_x \cdot l_y$ = 0.019*560*550 = 5852. In the reconstructed volume 35*151 = 5285 actual particles are counted between z = 35 and 185 voxels, which is in good agreement with the recorded number of particles. It is therefore concluded that the properties of the actual particles in the reconstructed volume can be inferred from a comparison of particles inside and outside the laser sheet.

The PDF of the particle peaks intensity (fig. 5-right) reveals that inside the light sheet the expected peak intensity is higher than outside, which means the real particles have a higher peak intensity compared to the ghost particles and reconstruction noise. This finding is in agreement with results of synthetic Tomographic-PIV experiments (Elsinga et al. 2006). From the figure it is concluded that the actual particles have an average peak intensity of 50 arbitrary units. Moreover figure 6 presents the effect of particle image density in *ppp* on the ghost and actual particle intensity. It is seen that the average peak intensity of the ghost particle increases with *ppp*, while the average intensity of the actual particles decreases slightly. Intensity is transferred from the actual particles to the ghosts.

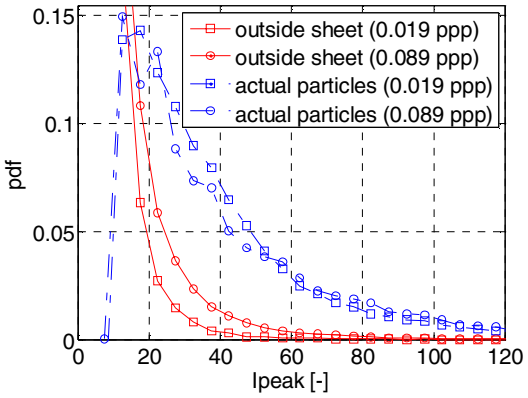

Figure 6: Comparison of the PDF of the peak intensity outside the light sheet and actual particles for an 8 mm thick light sheet and a seeding density of 0.019 and 0.089 ppp.

The ratio of actual tracer particles N_p and ghost particles N_g is determined at the average peak intensity of the actual particles (I_{peak} = 50). Figure 7 presents N_p/N_g versus the particle image density in the recorded particle images *ppp* for a light sheet thickness 4, 8 and 12 mm. The number of actual particles per ghost particle decreases with *ppp* and light sheet thickness as expected. The number of ghosts equals the number of actual particles at *ppp* = 0.15, 0.062 and 0.044 for light sheet thickness 4, 8 and 12 mm respectively. Furthermore $N_p/N_g \div ppp^{-3}$, as predicted for a 4-camera system (Eq. 3), is observed for $1< N_p/N_g <10$. In this range Eq. 3 is fit to the curves to obtain A_p (l_z is known from plots similar to fig. 5-left), which is found to increase with the light sheet thickness. It is believed

that this is due to the reduced signal-to-noise ratio in the recordings, which is not taken into account. The particle image intensity in the recordings reduces (fig. 8) due to the expansion of the light sheet with consequent drop in light intensity.

It is concluded that the maximum *ppp* still returning accurate reconstructions can be predicted a-priori using Eq. 3 with a reasonable estimate of the particle image area A_p. Alternatively figure 7 can be used directly for experimental configurations similar to the present one. Note that the present curve may depend on calibration accuracy and signal-to-noise ratio in the recorded images.

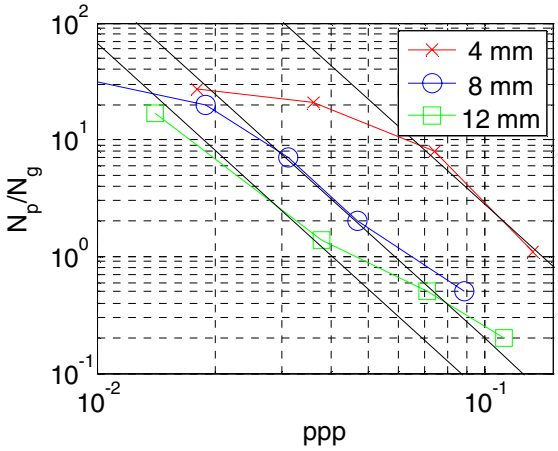

Figure 7: Ratio of actual tracer particle vs ghost particles for varying particle image density and light sheet thickness. Black lines indicate theoretical predictions.

Table 1: Parameters in fit Eq. 3 to curves in fig. 7

Light sheet thickness [mm]	l_z **[voxels]**	A_p **[pixels]**	**particle image radius [pixels]**
4	78	1.5	0.68
8	150	2.4	0.87
12	210	2.9	0.96

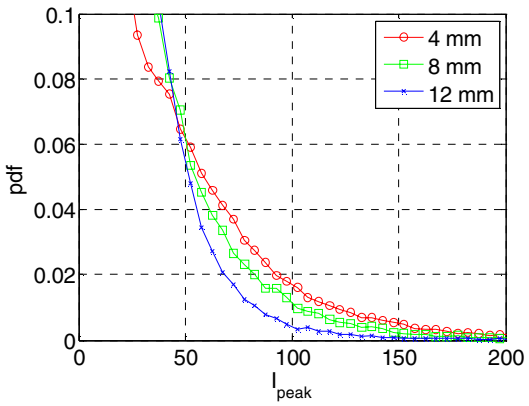

Figure 8: PDF of the peak intensity in the recordings for different light sheet thicknesses.

5. Assessment velocity accuracy

The velocity accuracy will be assessed based on the results for the 8 mm thick light sheet and considering three values for the recorded particle image density: 0.02, 0.05 and 0.08 *ppp*. The cross-correlation analysis returned 31x31x17 velocity vectors using an interrogation volume size of 41x41x21 voxels with 50% overlap. The velocity distribution averaged over 100 snapshots (fig. 9-right) is uniform along the cylinder axis, as expected, and shows a good qualitative agreement with stereo-PIV data (fig. 9-left). The quantitative comparison of the Tomographic-PIV and Stereo-PIV results in terms of mean and RMS flow velocity is discussed at the end of this section. Finally it is noted that the confidence level is approximately 80% for all cases (independent of the *ppp*).

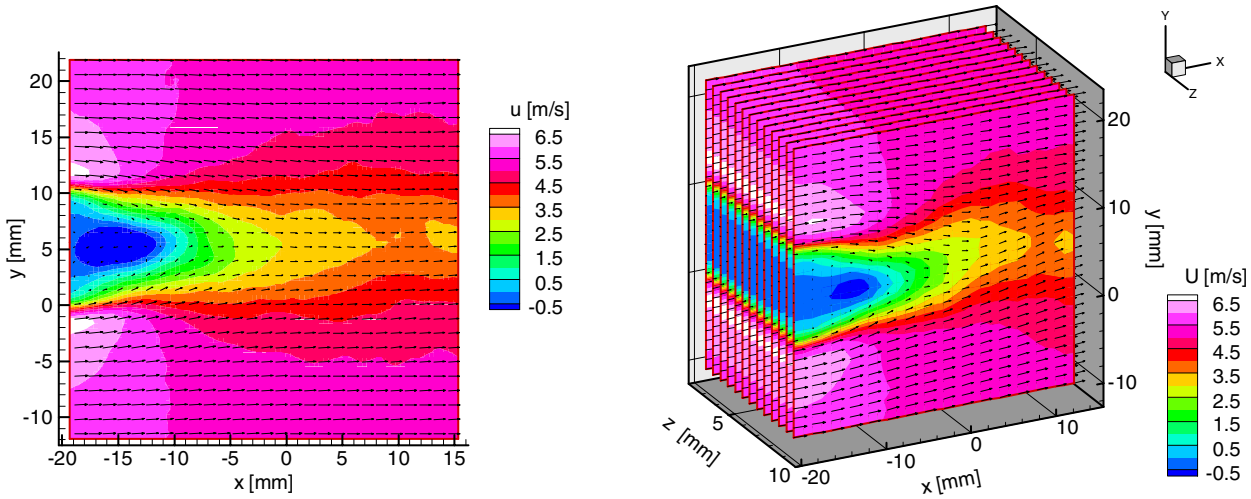

Figure 9: Mean velocity distribution obtained by Stereo (left) and Tomographic-PIV (8mm light sheet, right).

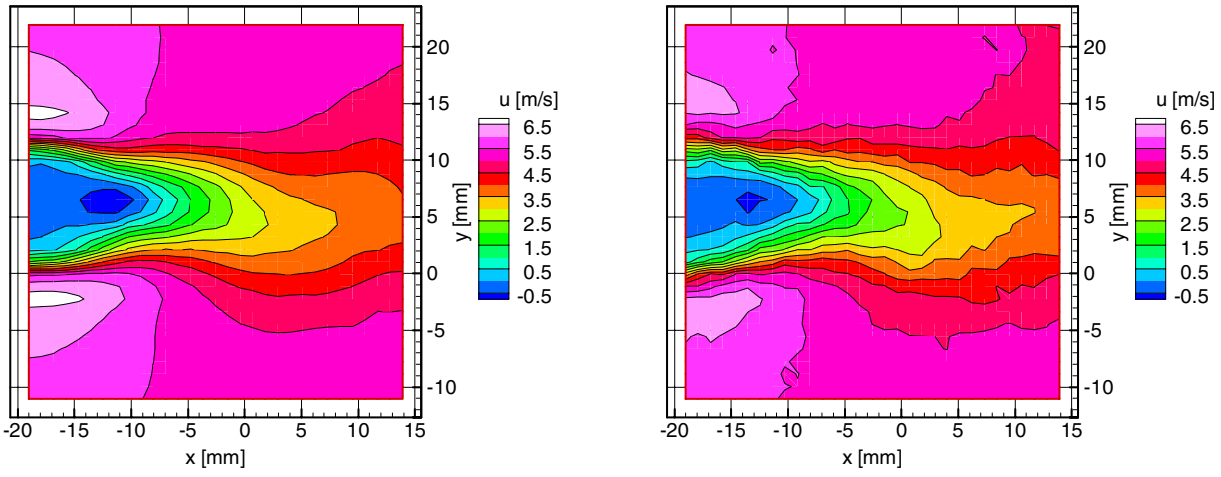

Figure 10: Mean velocity distribution inside (left) and outside laser sheet (right), (8mm light sheet and 0.05 ppp).

Figure 10 shows the mean velocity in slices of the measurement volume (constant z). The slice located inside the light sheet (fig. 10-left) clearly shows the two shear layers emanating from the upper and lower part of the cylinder. The shear layer reattach at x = -8.6 mm y = 6.4 mm enclosing

the circulation region with reversed flow. After the point of reattachment the width of the wake increases and the velocity deficit decreases. It is observed that the wake is not symmetrical as expected, which is most likely due to an insufficient number of samples. Finally the maximum value for the *u*-component of velocity is 6.6 m/s, which is found in the outer flow region.

The velocity distribution outside the light sheet (fig. 10-right) resulting from the cross-correlation of ghost particles (section 4), is similar to the velocity distribution inside. However, compared to inside the light sheet the velocity distribution is more smooth, which shows as an increase in the shear layer and wake thickness and a reduced peak velocity (positive as well as negative). To assess the contribution of the ghost particles to the velocity measurement, not only their velocity needs to be considered, but also the corresponding signal strength. The signal-to-noise ratio of the ghost velocity in the wake is 2.4 compared to 4.0 inside the laser sheet (fig. 11 and table 2). It is concluded that ghosts have a 'velocity' close to that of the actual tracer particles, hence may introduce a bias error in the velocity. However the amount of cross-correlation signal attributed to the ghosts is limited and therefore the bias is expected to be small.

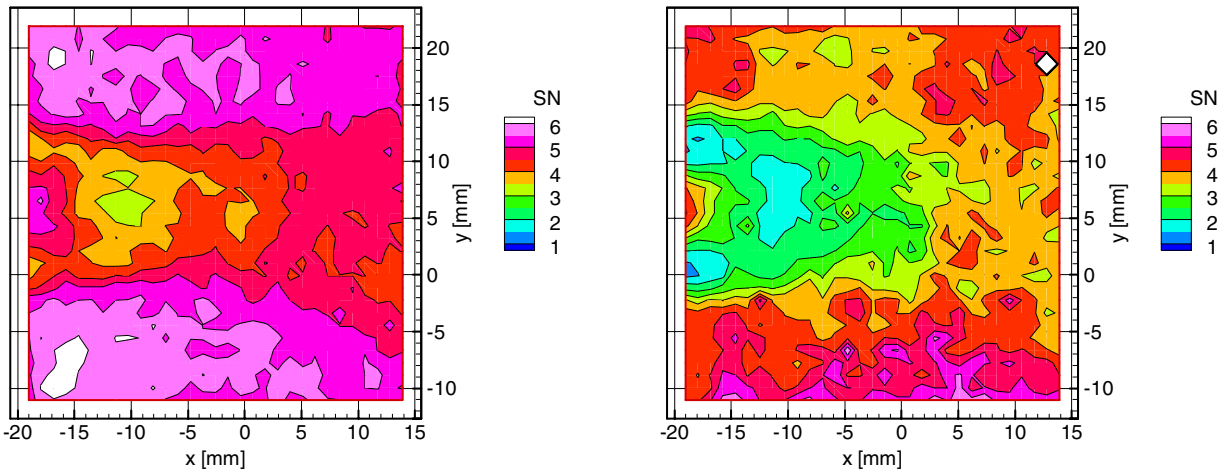

Figure 11: Cross-correlation signal-to-noise ratio distribution inside (left) and outside laser sheet (right), (8mm light sheet and 0.05 ppp).

Table 2: Cross-correlation signal-to-noise ratio at different locations in the volume

ppp	***actual particle per correlation volume***	***SN* in wake region**		***SN* in outer flow**	
		inside laser sheet	outside laser sheet	inside laser sheet	outside laser sheet
0.02	4.7	4.8	3.0	5.7	4.0
0.05	12	4.0	2.4	5.6	4.0
0.08	19	4.0	2.8	6.5	7.5

A model for the ghost particle velocity is offered in figure 12. A ghost particle is formed from 4 actual particles in a 4-camera system. In case the displacement between the 2 exposures is nearly equal for the 4 actual particles (within a particle image diameter, fig. 12-left), the ghost particle is formed in both exposures (from the same 4 actual particles) and is displaced by the average displacement of the 4 actual particles. As a result the ghost particles can cause velocity modulation, which is consistent with the smoothed velocity distribution observed in figure 10-right. If the

displacement from one of the 4 actual particles (the particle corresponding to cam4 in fig. 12-right) is different from the others, a ghost particle is returned in only one of the exposures, which does not contribute to the correlation peak.

The above model also offers an explanation for the high signal-to-noise ratio in the outer flow (table 2). The velocity variations in that region are small and therefore the majority of the ghost particles are expected to be in both exposures and contribute to the correlation. For 0.08 *ppp* the signal-to-noise ratio outside the laser sheet (the ghost particles) is even higher than inside the laser sheet. Alternatively the velocity fluctuations in the wake region are much higher and the flow is more three-dimensional. Consequently fewer ghost particles return in both exposures and contribute to a correlation peak. Therefore the signal-to-noise ratio in the wake region is lower, especially outside the laser sheet (associated to the ghost particles).

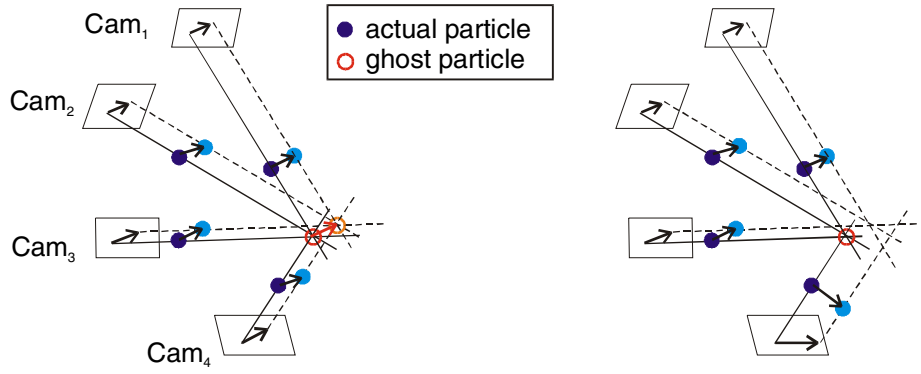

Figure 12: Formation of ghost particles that contribute to the cross-correlation (left) and non-correlating ghost particle (right). Dark particles and solid lines-of-sight correspond to the first exposure. Bright particles and dashed lines-of-sight correspond to the second exposure.

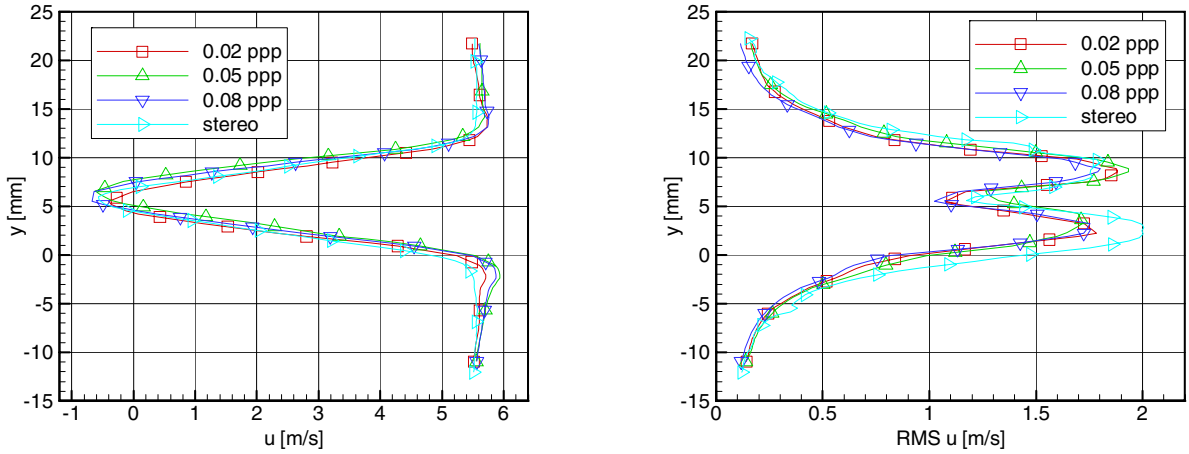

Figure 13: Profiles of the u-component of velocity at x = -10 mm, mean (left) and RMS (right). Comparing Tomographic-PIV at different seeding densities with Stereo-PIV.

Finally a quantitative comparison between Tomographic-PIV and Stereo-PIV is presented in figure 13. The mean profile of the *u*-component of velocity (fig. 13-left) agrees within 0.50 m/s (corresponding to 0.30 voxel particle displacement). The RMS profile of the *u*-component also demonstrates good agreement between the two techniques. In the lower part of the wake Stereo-PIV

returns higher RMS. The maximum difference is 0.3 m/s or 0.18 voxel particle displacement at y = -2.5 mm. The Tomographic-PIV results for different seeding densities do not show a significant difference. It is therefore again concluded that the contribution of the ghost particles to the velocity measurement is limited. Even if the number of ghost particles in the volume is larger than the number of actual tracer particles as is the case for 0.08 *ppp*.

6. Conclusions

The accuracy of Tomographic-PIV was assessed experimentally based on measurements of a circular cylinder wake flow at Re_D = 2700, which were carried out for a light sheet thickness of 2, 4, 8 and 12 mm and seeding density ranging from 0.01 to 0.1 *ppp*. Both the accuracy of the 3D particle reconstruction and velocity measurement were considered. The experimental setup consisted of a four camera imaging system with a maximum angle between viewing directions of 45 degrees and a slit to set the light sheet thickness and to sharply define its position in depth.

A procedure was described to quantify reconstruction noise (in the form of ghost particles) in Tomographic-PIV experiments, which applied to the present measurements returned the reconstruction signal-to-noise ratio as a function of light sheet thickness and seeding density (fig. 7). The results were in good agreement with a predictive model (section 2), so that in future experiments the reconstruction accuracy can be estimated a priori.

The accuracy of the measured velocity is assessed by a comparison with Stereo-PIV. It was shown that the mean and RMS velocity agree within 0.5 and 0.3 m/s respectively (corresponding to 0.30 and 0.18 voxel particle displacement). Furthermore it was found that reconstruction noise or ghost particles have a limited effect on the cross-correlation. For the range of particle image seeding densities considered (0.02 to 0.08 *ppp*) no significant difference in the returned flow statistics was observed, even though the number of ghost particles exceeded the number of actual particle for 0.08 *ppp*. Moreover a model to describe the influence of ghost particles on the velocity measurement was presented.

Acknowledgement

B. Wieneke and D. Michaelis from LaVision GmbH are kindly acknowledged for the hardware and software support to the present Tomographic-PIV experiments.

References

Brücker Ch (1995) Digital-Particle-Image-Velocimetry (DPIV) in a scanning light-sheet: 3D starting flow around a short cylinder. *Exp Fluids* 19: 255-263

Elsinga GE, Scarano F, Wieneke B, van Oudheusden BW (2005a) Tomographic particle image velocimetry. *6th Int Symp on Particle Image Velocimetry*, Pasadena, CA, USA

Elsinga GE, Wieneke B, Scarano F, van Oudheusden BW (2005b) Assessment of Tomo-PIV for three-dimensional flows. *6th Int Symp on Particle Image Velocimetry*, Pasadena, CA, USA

Elsinga GE, Scarano F, Wieneke B, van Oudheusden BW (2006) Tomographic particle image velocimetry. *Submitted to Exp Fluids*

Hinsch KD (2002) Holographic particle image velocimetry. *Meas Sci Technol* 13: R61-R72

Maas HG, Gruen A, Papantoniou D (1993) Particle tracking velocimetry in three-dimensional flows. *Exp Fluids* 15: 133-146

Scarano F, Riethmuller ML (2000) Advances in iterative multigrid PIV image processing. *Exp Fluids* 29: S051

Wieneke B (2005) Stereo-PIV using self-calibration on particle images. *Exp Fluids* 39: 267-280